Earth Planet. Sci. Lett. 679 (2026) 119860

Contents lists available at ScienceDirect

Earth and Planetary Science Letters

journal homepage: www.elsevier.com/locate/epsl

Induced seismicity in the southern Sichuan basin regulated by heterogeneous folding

Bingfeng Zhang [a,b], Xuewei Bao [a,*], Mengfan Jiang [a], Kecheng Zhou [a]

[a] Key Laboratory of Geoscience Big Data and Deep Resource of Zhejiang Province, School of Earth Sciences, Zhejiang University, Hangzhou 310058, China
[b] Division of Mathematical Sciences, School of Physical and Mathematical Sciences, Nanyang Technological University, Singapore, 639798, Singapore

ARTICLE INFO

Editor: Dr H Thybo.

Keywords:
Induced seismicity
Sichuan basin
Shale gas field
Seismogenic environment
Seismic tomography
Moment tensor

ABSTRACT

The potential for strong induced earthquakes in industrial production fields is largely controlled by the spatial arrangement of pre-existing faults shaped by regional tectonics. The 2021 Ms 6.0 Luxian earthquake in the southern Sichuan basin is an unusual case in which the seismogenic fault geometry deviates from the prevailing regional stress field and geological framework. To date, the seismogenic environment and the tectonic processes responsible for this destructive event remain poorly understood. In this study, we present a sedimentary shear-wave velocity model and eleven moment tensor solutions across the Luxian shale gas field, derived using data collected by our newly deployed seismic network. Our results reveal previously unrecognized, nearly reversed lateral variations in the amplitudes of synclinal low-velocity anomalies between terrestrial and marine strata, in addition to a first-order velocity contrast that correlates with the regional anticline–syncline architecture. The central Yujiasi syncline exhibits weaker low-velocity anomalies in the shallow terrestrial strata than areas to the north and south, reflecting lower strain intensity likely influenced by shallower décollement layers. Detected seismicity and anomalous reverse-faulting events with fold-parallel P-axes (including the Ms 6.0 earthquake) cluster mainly within two strain transition zones of the Yujiasi syncline, where stress is expected to concentrate and form fold-normal fault planes. These observations provide direct evidence that heterogeneous folding regulates the spatial distribution of induced seismicity in the southern Sichuan basin. They also help identify areas susceptible to induced seismic hazards and provide guidance for planning hydraulic fracturing operations in the region.

1. Introduction

On 15 September 2021 (UTC), a destructive Ms 6.0 (Mw 5.4) earthquake struck Luxian County, Sichuan Province, China, causing three fatalities, 159 injuries, and severe damage to buildings and transportation infrastructure (Li et al., 2022). This event heightened public concern about seismic hazards in the region. Geographically, Luxian County lies within the tectonically stable interior of the Sichuan basin (Fig. 1), where large-magnitude tectonic earthquakes have historically been rare, but induced seismicity spanning a wide range of magnitudes has been frequent in recent decades. Wastewater injection operations in the adjacent Rongchang District were responsible for the increased seismicity in the northwestern part of the county between 1988 and 2013 (Lei et al., 2008; Li et al., 2022; Zuo and Zhao, 2023). Beginning in 2020, earthquake frequency rose again (Fig. 2a), accompanied by several moderate-to-large-magnitude events. This surge coincided with the onset of extensive shale gas exploration throughout the county and is spatially correlated with well pads and/or nearby faults (Cai et al., 2024; Li et al., 2022; Yin et al., 2025; Zuo and Zhao, 2023).

The Sichuan basin and its surroundings constitute China's the most critical shale gas production district (Wu et al., 2025). By 2023, cumulative proven shale gas reserves in the Wufeng–Longmaxi Formation of the Sichuan basin had reached 2.96 trillion m^3, with annual production exceeding 25 billion m^3 (Nie et al., 2024). The Luzhou shale gas block lies closer to the regional depocenter of the Wufeng–Longmaxi Formation than the nearby Changning–Weiyuan blocks and contains the thickest (500–650 m) and deepest (>3500 m) gas-bearing strata in the area (Yang et al., 2019). Key reservoir properties, including high brittle mineral content, elevated formation pressure, and high gas saturation, make the Luzhou block particularly favorable for shale gas enrichment and high productivity (Yang et al., 2019). Shale gas exploration in

* Corresponding author.
E-mail address: xwbao@zju.edu.cn (X. Bao).

https://doi.org/10.1016/j.epsl.2026.119860
Received 27 September 2025; Received in revised form 12 January 2026; Accepted 15 January 2026
Available online 23 January 2026

Luxian County holds strategic significance for China's national energy security and low carbon economy, and the 2021 Ms 6.0 earthquake may not represent an isolated "dragon-king" event. Large-magnitude earthquakes induced by industrial activities are well documented worldwide (e.g., the 2016 Mw 5.8 Oklahoma earthquake; Grandin et al., 2017) and have become increasingly frequent in the southern Sichuan basin in recent years (Lei et al., 2020) (Fig. 1a). The associated secondary geological hazards, including post-earthquake landslides, gas leakage, and wildfires, pose additional risks (Liu et al., 2024b). Understanding the seismogenic environment of the Luxian shale gas field is thus essential for mitigating seismic hazards associated with hydraulic fracturing operations, ensuring the safety and sustainability of shale gas extraction, and improving our understanding of the mechanisms that generate large-magnitude induced earthquakes (Keranen and Weingarten, 2018; Zhou et al., 2024).

Geologically, Luxian County lies at the broom-shaped southwestern tip of the northeast-trending eastern Sichuan fold-and-thrust belt (Fig. 1a). This thin-skinned belt began developing in the Cretaceous, driven by westward subduction of the Pacific Plate, and is characterized by dominant northwestward thrusting and southeastward back-thrusting within the sedimentary cover (Li et al., 2015). Subsequently, during ~20–10 Ma, the belt underwent reversed southeastward thrusting and regional uplift in response to the India–Eurasia collision (Li et al., 2015). The study area contains a series of NNE-oriented Jura-type ejective folds with narrow chevron anticlines and broad box synclines, including the Luoguanshan, Gufoshan, Jiukuishan, and Longdongping anticlines and the Yujiasi and Desheng synclines (Fig. 1b). Shallow-crustal stratigraphy is divided into three main groups (from bottom to top; Fig. 2c): the Pre-Sinian Banxi Group basement, consisting of a suite of metamorphic and igneous rocks; the Middle Triassic to Sinian marine sequence, composed mainly of carbonates interbedded with mudstone, shale, sandstone, and siltstone; and the Upper Triassic to Jurassic terrestrial sequence, comprising mudstone and sandstone (Li et al., 2015; Tian et al., 2024a). Key décollement layers include the Middle–Lower Cambrian mudstone, shale, and gypsum–salt rocks; the Silurian mudstone and shale; and the Upper Permian–Lower Triassic coal and gypsum rocks (Tian et al., 2024a). Fold-accommodation faults are widespread between these marine décollement horizons but are concentrated mainly in anticlinal zones within the overlying terrestrial strata (Tian et al., 2024a).

Geophysical investigations in earthquake-prone regions can illuminate seismicity characteristics and subsurface structural heterogeneity, offering key insights into the seismogenic environment of large earthquakes. Previous studies indicate that the 2021 Luxian Ms 6.0 earthquake occurred on a blind fault within the Yujiasi syncline (China Earthquake Networks Center epicenter: 105.34°E, 29.20°N), with focal and centroid depths of ~4–6 km in the marine sedimentary strata (Li et al., 2022; Lu et al., 2024; Mo et al., 2024; Yi et al., 2021; Zhao et al., 2023b). Seismic waveform inversions and InSAR analyses show that it was a reverse-faulting event with a minor sinistral strike-slip component (strike: NWW–SEE; dip: ~45°) (Mo et al., 2024; Zhao et al., 2023b). This fault plane solution differs from those of most moderate earthquakes in the area (Li et al., 2022) and is inconsistent with the regional maximum horizontal compressive stress (SHmax, NWW–SSE; Heidbach et al.,

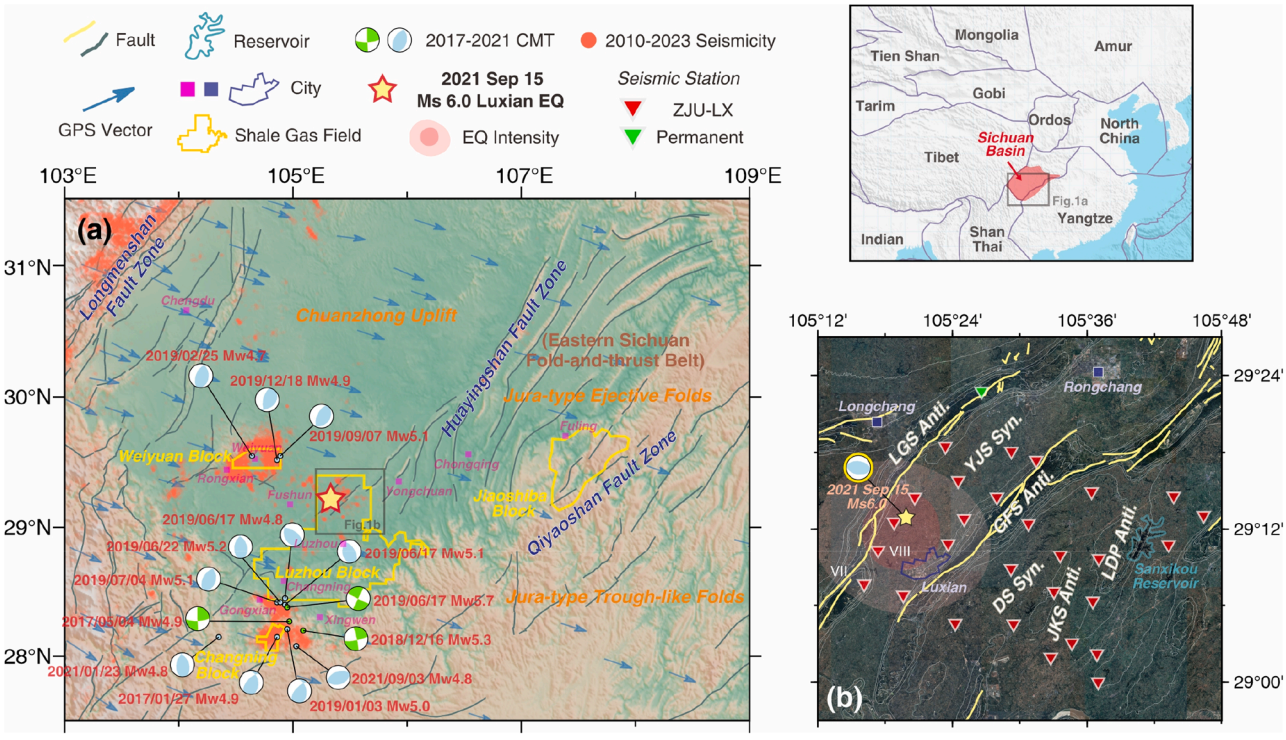

Fig. 1. Tectonic and seismogenic settings of the study area. (a) Seismotectonics of the southern Sichuan basin. Yellow star shows the centroid of the 2021 Ms 6.0 Luxian earthquake (Zhao et al., 2023b). Orange dots mark the 2010–2023 relocated earthquake catalog for Sichuan Province, China (Zhao, 2024). Focal mechanisms of 14 Mw > 4.5 earthquakes since 2017 (from GCMT) are colored by type: light blue for reverse faulting and green for strike-slip faulting. Yellow polygons denote major shale gas blocks. Blue arrows indicate GPS velocities relative to stable Eurasia (Wang and Shen, 2020). The eastern Sichuan fold-and-thrust belt, bounded by the Huayingshan and Qiyaoshan fault zones, is characterized by ejective folds, in contrast to the trough-like folds southwest of the Qiyaoshan Fault. Luxian County, the study region, lies at the broom-shaped southwestern tip of the belt. The inset map (upper right) shows the tectonic context of the Sichuan basin (Hasterok et al., 2022). **(b)** Zoomed-in satellite image of Luxian County. The broadband seismic stations used in this study are denoted by color-filled inverted triangles. The focal mechanism (Zhao et al., 2023b) and intensity map (Mo et al., 2024) of the Ms 6.0 mainshock are indicated. The Sanxikou reservoir is outlined in cyan. Folding configurations (thin white lines in panel b) and fault traces are from the China National Digital Geological Map (1:200,000) and the China Active Faults Database (Wu et al., 2024b). Abbreviations: LGS = Luoguanshan, YJS = Yujiasi, GFS = Gufoshan, DS = Desheng, JKS = Jiukuishan, LDP = Longdongping, Syn. = Syncline, Anti. = Anticline.

2018) (Fig. 2b). The core area of the mainshock rupture zone is ~5 km long at 4–6 km depth, lying beneath the shale gas reservoir and intersecting well pad H79, which was undergoing hydraulic fracturing before the event, suggesting that fluid infiltration contributed to its nucleation (Zhao et al., 2023b). The earthquake produced minor line-of-sight coseismic surface displacements of up to 3.6 cm and >3000 aftershocks, likely triggered by coseismic stress transfer and fluid diffusion (Guo et al., 2025; Wang et al., 2023; Zhao et al., 2023b; Zhu et al., 2025). The fold-normal, stress-parallel seismogenic fault distinguishes the Luxian earthquake from other major induced events in the southern Sichuan basin, such as those in the Changning anticline (Li et al., 2023; Lu et al., 2021; Tan et al., 2020) and the Weiyuan anticline (Liu et al., 2023; Sheng et al., 2022; Song et al., 2025; Wang et al., 2020; Zi et al., 2025), where slip primarily occurred on pre-existing basement faults favored by the regional stress field. This contrast underscores the significance of the Luxian earthquake for understanding seismic potential in the southern Sichuan basin.

In Luxian County, the stratigraphic positions of the sedimentary cover have been well mapped by active-source seismic reflection surveys (Lu et al., 2024; Tian et al., 2024a). Information on seismic velocity structures is available from several passive-source tomographic studies (Cai et al., 2024; Chen et al., 2022; Wu et al., 2024a, 2023; Xu et al., 2023; Zuo and Zhao, 2023), most of which use regional networks or short-period data and focus on the Ms 6.0 earthquake source region. Different scenarios have been proposed for the preferred locations of local seismicity: within high-velocity, low-Vp/Vs zones (Cai et al., 2024); along the boundaries between high- and low-velocity zones (Zuo and Zhao, 2023); or a combination of both (Chen et al., 2022; Wu et al., 2024a, 2023; Xu et al., 2023). The 2021 Ms 6.0 mainshock has also been linked to the intersection of high- and low-resistivity zones (Liu et al.,

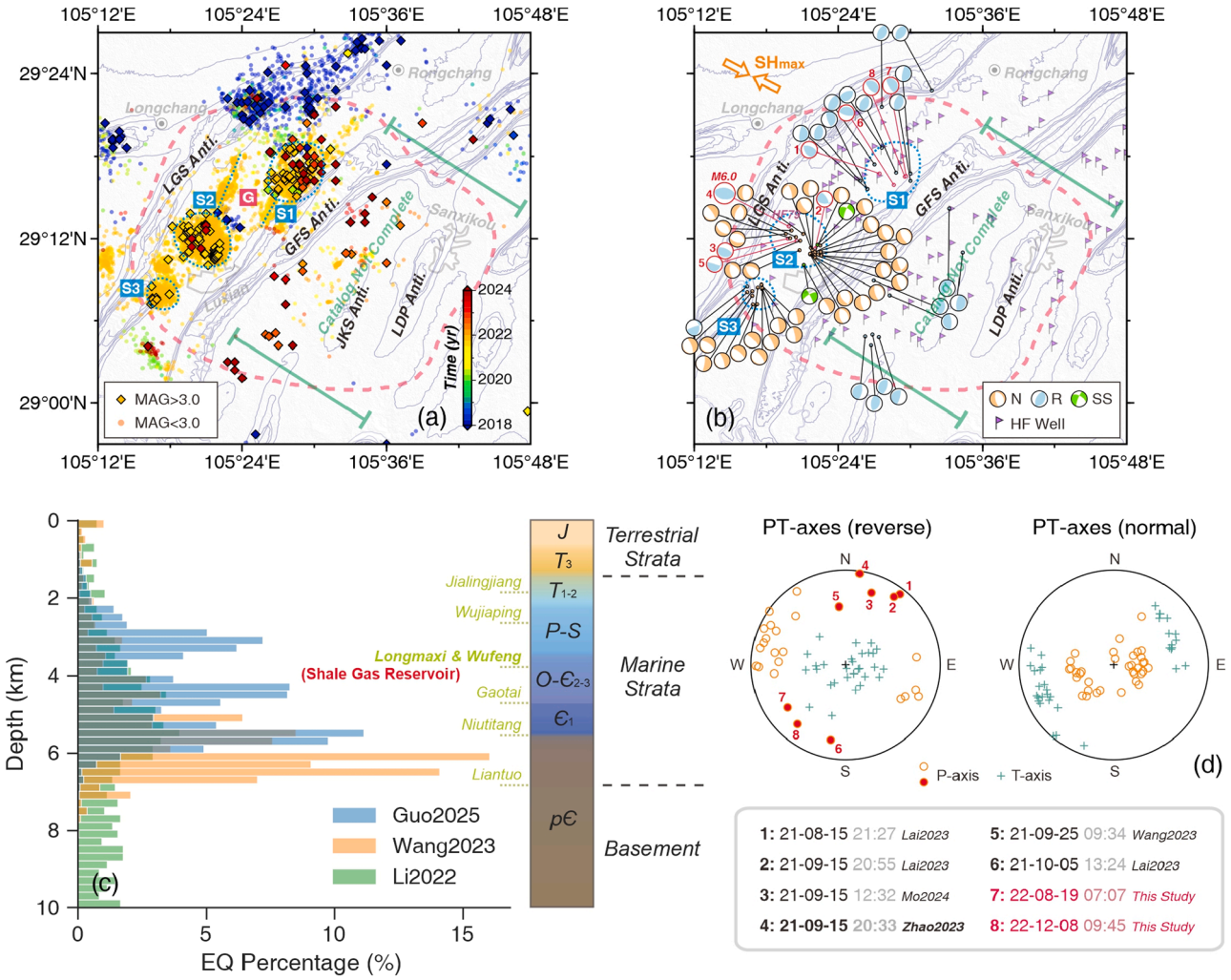

Fig. 2. Seismicity distribution and focal mechanisms. (a) Local seismicity compiled from previous studies (Guo et al., 2025; Li et al., 2022; Wang et al., 2023; Zhao, 2024) and the China Earthquake Networks Center catalog, colored by origin time. Earthquakes with $M > 3$ are shown as diamonds and those with $M < 3$ as dots. Three major seismic clusters (S1, S2, S3) and a seismic gap (G) in the Yujiasi syncline are indicated. Seismicity in the Desheng syncline remains incompletely cataloged. The well-resolved region of the tomographic model is outlined by dashed pink lines. **(b)** Focal mechanisms from this and previous studies (Lai et al., 2023; Li et al., 2022; Mo et al., 2024; Wang et al., 2023; Yi et al., 2021; Zhao et al., 2023b). Eight reverse-faulting events with anomalous fold-parallel P-axes are highlighted with red circles. Hydraulic fracturing wells are marked by purple flags, with well pad H79 adjacent to the Ms 6.0 mainshock labeled. Regional SHmax orientation (Heidbach et al., 2018) is shown at upper left. **(c)** Depth distribution of seismicity (in percentage) for three catalogs (Guo et al., 2025; Li et al., 2022; Wang et al., 2023). The stratigraphic column is based on seismic reflection profiles within the Yujiasi syncline (Lu et al., 2024). $p\mathcal{E}$, Precambrian; $\mathcal{E}_1$, Lower Cambrian; $\mathcal{E}_{2-3}$, Upper–Middle Cambrian; *O*, Ordovician; *S*, Silurian; *P*, Permian; T_{1-2}, Lower–Middle Triassic; T_3, Upper Triassic; *J*, Jurassic. Representative sedimentary formations are labeled (Tian et al., 2024a). Major décollement layers occur in gypsum- or coal-bearing Gaotai, Wujiaping, and Jialingjiang formations, with additional local décollements in shale- or mudstone-bearing units (e.g., Niutitang, Wufeng, Longmaxi). **(d)** Polar plots of P- and T-axes for reverse- and normal-faulting mechanisms. Eight reverse-faulting events with anomalous fold-parallel P-axes are highlighted and labeled. Abbreviations: Anti. = Anticline; Syn. = Syncline; *R* = Reverse; *N* = Normal; SS = Strike-Slip.

2024a) and of contrasting magnetic susceptibility (Zhao et al., 2023a). Such geophysical anomalies often reflect structural heterogeneities, and the boundaries between high- and low-anomaly zones commonly mark strong contrasts in physical properties. However, the tectonic processes that produce these potential associations between geophysical anomalies and earthquake occurrence in the Luxian area remain elusive.

In this study, to gain insights into the seismogenic environment of Luxian shale gas field and the tectonic processes influencing regional susceptibility to induced earthquakes, we determine the shear-wave velocity structure of the sedimentary cover using ambient noise tomography and analyze source characteristics through moment tensor inversion, based on data from our newly deployed county-wide broadband seismic network. Our observations delineate a clear clustering of hydraulic-fracturing–induced seismicity around the margins of low-velocity zones in the marine strata, highlighting the key role of local heterogeneous folding in regulating seismic potential in the southern Sichuan basin.

2. Data and methods

2.1. Ambient noise data and Rayleigh-wave dispersions

We deployed a portable seismic array (ZJU–LX; 28 stations) across Luxian County from August 2022 to June 2023, with an average inter-station spacing of ~5 km (Fig. 1b). Each site was equipped with a Nanometrics Trillium Horizon broadband seismometer and a Centaur-3 digitizer, sampling at 100 Hz. Data from station CQ.ROC of the Chinese provincial seismic network were also incorporated into the analyses.

We process vertical-component ambient noise data recorded by the aforementioned seismic stations to extract inter-station empirical Green's functions following the methodology of Bensen et al. (2007). The main processing steps include: (1) segmenting and resampling waveforms into one-hour segments with 30-minute overlap and at 20 Hz, (2) removing the instrument response, (3) applying a band-pass filter (0.2–15 s), (4) performing time- and frequency-domain whitening, (5) conducting waveform cross correlation between all synchronous stations, and (6) "robust-stacking" all hour-long inter-station cross correlations (Pavlis and Vernon, 2010). Fundamental-mode Rayleigh-wave phase traveltimes in the period range 0.5–12 s are then measured using Automatic Frequency–Time Analysis (Bensen et al., 2007). We select high-quality traveltimes for subsequent tomographic inversions based on the following criteria: (1) a minimum signal-to-noise ratio (SNR) of 5, (2) inter-station distances greater than 1.5 wavelengths at the corresponding period, and (3) removal of outliers exceeding 2.5 standard deviations from the mean. Detailed statistics of the ambient noise dataset are provided in Fig. S1.

2.2. Direct inversion for 3-D shear-wave velocity

We employ a novel direct surface-wave inversion technique (DSurfTomo; Fang et al., 2015), which bypasses the intermediate construction of 2-D phase velocity maps, to invert for 3-D shear-wave velocity at 0–6 km depths. The principle of this method is to minimize the phase traveltime residuals between observations $T^o_{f,i}$ and model predictions $T_{f,i}$ for all frequencies ($f = 1,2,\ldots, N_f$) and all station pairs ($i = 1,2,\ldots, N_s$) simultaneously. Under the high-frequency approximation (ray theory), the traveltime residual $\delta T_{f,i}$ for the i-th station pair at the f-th frequency is expressed as:

$$\delta T_{f,i} = T^o_{f,i} - T_{f,i} = -\sum_{k=1}^{N_k} v_{i,k}\frac{\delta C_{f,k}}{C^2_{f,k}} = -\sum_{k=1}^{N_k}\frac{v_{i,k}}{C^2_{f,k}}\sum_{j=1}^{N_j}\left[R_{\alpha|\beta}\frac{\partial C_{f,k}}{\partial \alpha_{j,k}} + \frac{\partial C_{f,k}}{\partial \beta_{j,k}} + R_{\rho|\beta}\frac{\partial C_{f,k}}{\partial \rho_{j,k}}\right]\delta\beta_{j,k}, \quad (1)$$

where N_k and N_j are the quantities of horizontal and vertical grid nodes, respectively; $v_{i,k}$ is the interpolation coefficient for the k-th horizontal grid node associated with the i-th station pair; $C_{f,k}$ and $\delta C_{f,k}$ are the phase velocity of the k-th horizontal grid node at the f-th frequency (calculated using the node-specific shear-velocity profile; Herrmann, 2013) and its perturbation, $R_{\alpha|\beta}$ and $R_{\rho|\beta}$ are empirical relationships relating Vp (α) and density (ρ) to Vs (β). Vp and density are coupled to Vs because their sensitivity kernels are non-negligible, yet challenging to resolve independently from surface wave data (Hao et al., 2024). Synthetic traveltimes and ray paths are calculated using the fast marching method (Rawlinson and Sambridge, 2004), while depth sensitivity kernels ($\partial C_{f,k}/\partial \alpha_{j,k}$, $\partial C_{f,k}/\partial \beta_{j,k}$, $\partial C_{f,k}/\partial \rho_{j,k}$) are computed using a difference approach. Eq. (1) can also be expressed in a simplified matrix form as $\boldsymbol{d} = \boldsymbol{Gm}$, where $\boldsymbol{d}$ is the residual vector, $\boldsymbol{G}$ the data sensitivity matrix, and $\boldsymbol{m}$ the model perturbation vector. The solution is obtained by minimizing:

$$\min_{\boldsymbol{m}}\chi(\boldsymbol{m}) = \| \boldsymbol{d} - \boldsymbol{Gm} \|_2^2 + \lambda \| \boldsymbol{Lm} \|_2^2, \quad (2)$$

using the LSQR algorithm (Paige and Saunders, 1982), where $\boldsymbol{L}$ is a model smoothing operator and λ is a weighting parameter balancing data fitting and model regularization. The shear-wave velocity model is iteratively updated and optimized using the solution of Eq. (2) (i.e., $\boldsymbol{m}$). Synthetic traveltimes, ray paths, and depth sensitivity kernels are also updated through the iterations accordingly.

During the inversion, the study area (105.19°E–105.85°E, 28.95°N–29.46°N, 0–20 km depth) is discretized into a 23 × 18 × 16 mesh, comprising a regular horizontal grid with 0.03° spacing and a flexible vertical grid at 0.0, 0.5, 1.0, 1.5, 2.0, 2.5, 3.0, 4.0, 5.0, 6.0, 7.5, 9.0, 10.5, 12.0, 15.0, and 20.0 km. The input dataset includes 5245 high-quality Rayleigh-wave phase traveltimes from 310 station pairs, covering the period range 1–8 s in 0.2 s increments. A 1-D shear-wave velocity profile, obtained by inverting the average dispersion curve using the evolutionary algorithm (Luu, 2023), serves as the starting model for the 3-D inversion. The weighting parameter λ is optimally set to 9 based on L-curve analysis, and the maximum number of iterations is set to 10. Depth sensitivity kernels, the initial model, and L-curve illustrations are provided in Figs. S2–S4.

2.3. Centroid moment tensor inversion

Thirteen earthquakes with M > 2.5 occurred in Luxian County during the operation of the ZJU–LX array, according to the provincial catalog (Zhao, 2024). All these events generated clear seismic signals that were readily distinguishable from background noise and consistently recorded at a large number of operating stations. We computed their centroid moment tensor (CMT) solutions using the ISOLA method (Sokos and Zahradnik, 2008; Vackář et al., 2017), which combines least-squares inversion for MT parameters and a grid search over centroid time and location. For each candidate time–space grid point, an optimal MT solution is obtained by minimizing the standardized misfit between observed and synthetic waveforms. A data covariance matrix derived from pre-event noise and representing data uncertainty, is incorporated into the misfit function to preferentially weight high-SNR frequency bands in the inversion. The final CMT solution for each event is selected as the grid point with the smallest misfit. Here, seismograms are corrected for instrument response and band-pass filtered between 0.05 and 0.20 Hz, while Green's functions are calculated using the discrete wavenumber method (Bouchon, 1981) and the regional average Vs profile from the tomographic inversions. Figures S5–S9 provide inversion statistics and waveform fits for events with M > 3.5 and those exhibiting high non-DC components. The uncertainty of the MT solutions is evaluated through four sets of robustness tests described in Section 3.3.

3. Results

3.1. Tomographic inversion stability and resolution tests

As shown in Fig. S4, the root-mean-square phase traveltime residual decreases rapidly from 0.43 s to 0.31 s during the first three iterations and converges to 0.30 s after the tenth iteration, indicating a good fit to the observational data. To further evaluate the stability of the imaging results, we performed additional inversions using the same parameters but different initial models (Fig. S3). Two alternative initial models were tested: (1) a mixed shear-wave velocity profile (A-1) constructed from phase-velocity–converted Vs at 0–8 km (Fang et al., 2015) combined with the Vs from Bao et al. (2015) at greater depths, and (2) a regional average Vs profile for the western part of Luxian County (A-2) (Xu et al., 2023). Both tests yield results that are highly consistent with the final model, particularly in terms of the velocity perturbation patterns discussed in the main text with average absolute deviations of ~0.3–0.6 % and local maxima generally not exceeding ~1–2 % (Fig. S10). Furthermore, the model features are robust with respect to the choice of dispersion sampling and inversion grid (Fig. S11).

The resolving capability of the seismic data and inversion scheme was quantitatively assessed with checkerboard resolution tests. Three layers (0–2 km, 2.5–6 km, and 7.5–20 km) of alternating checkered perturbations with ~12 km lateral cell size were superimposed on the initial model. Synthetic traveltimes were generated from the target model and then contaminated with 1.2 % random Gaussian noise, as is commonly adopted in ambient noise tomography studies. Data configurations and inversion parameters were kept consistent with those used in the real-data inversion. The results show that velocity anomalies above 6 km depth are satisfactorily recovered in regions of adequate data coverage, which are outlined by dashed lines in Fig. S12 and described in the following sections.

3.2. 3-D shear-wave velocity structure

Our seismic images reveal the structural attributes of the sedimentary cover (0–6 km depth) in Luxian County. The mapped shear-wave velocity heterogeneities align closely with the local tectonic framework, displaying dominant low-velocity anomalies (L1, L2) beneath the Yujiasi and Desheng synclines and high-velocity anomalies (H1, H2, H3) beneath the Luoguanshan, Gufoshan, and Jiukuishan–Longdongping anticlines (Figs. 3 and 4). Lateral and vertical variations in the shape and

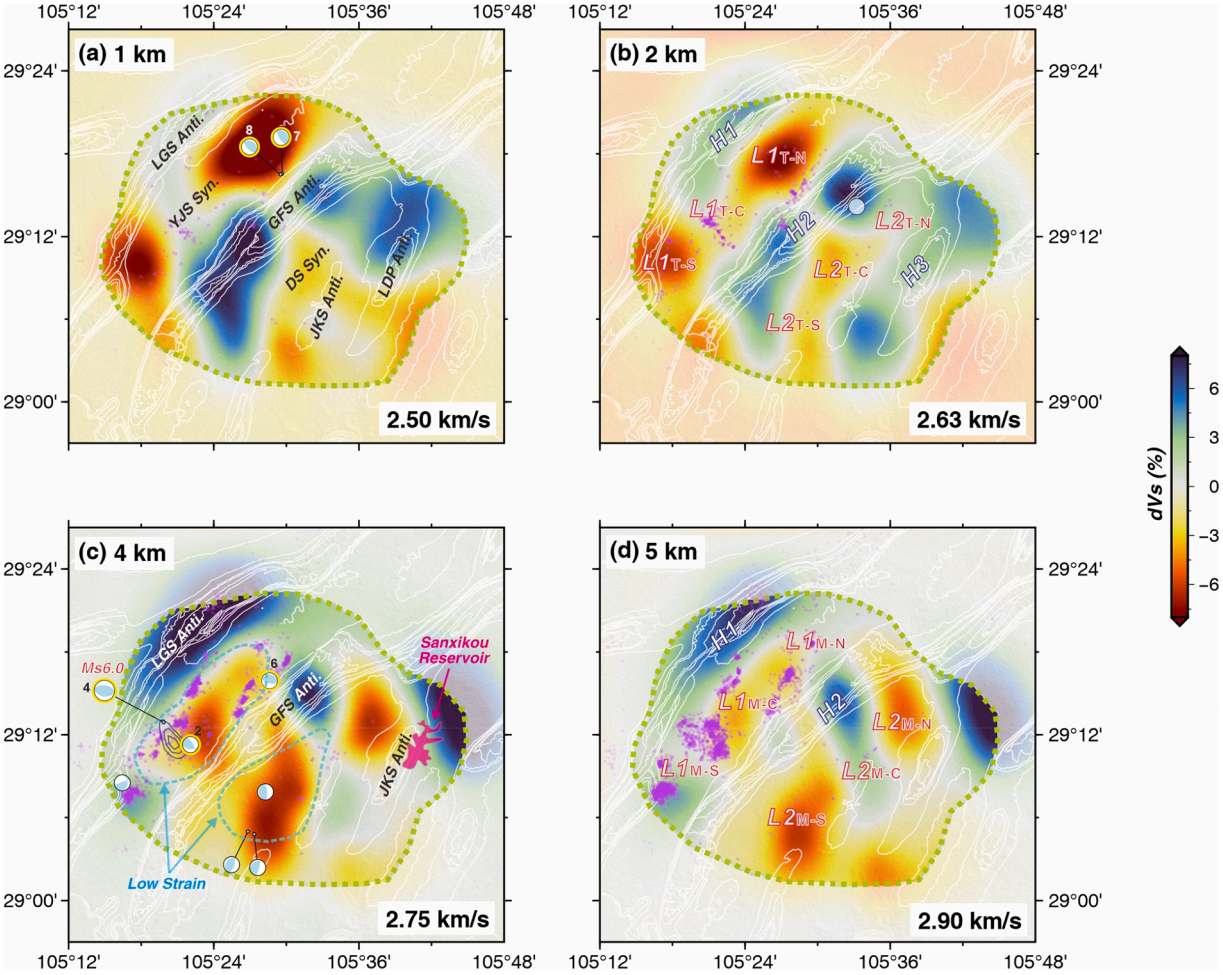

Fig. 3. Seismic tomographic images of sedimentary layers in Luxian County (horizontal slices). S-wave velocity perturbations at 1, 2, 4, and 5 km depth are shown. Well-resolved regions, delineated by checkerboard resolution tests, are outlined with dashed green lines. Purple dots and beachballs mark regional seismicity and reverse-faulting focal mechanisms within ±0.5 km of each target depth (this study; Guo et al., 2025; Li et al., 2022; Wang et al., 2023; Zhao, 2024). Focal mechanisms with anomalous fold-parallel P-axes are numbered as in Fig. 2. Areas of previously reported low strain intensity (Wu et al., 2024a; Yang et al., 2019) are outlined with light-blue dashed lines in panel (c). The main slip zone of the 2021 Ms 6.0 mainshock (Zhao et al., 2023b) is indicated by gray elliptical contours in panel (c). Regional anticline–syncline traces are shown as thin white lines in the background. Prominent anomalies discussed in the text are labeled in panels (b) and (d). Low-velocity anomalies follow the notation L_{ij-k}, where i is the anomaly index, j denotes the terrestrial (T) or marine (M) stratigraphic level, and k indicates the northern (N), central (C), or southern (S) segment.

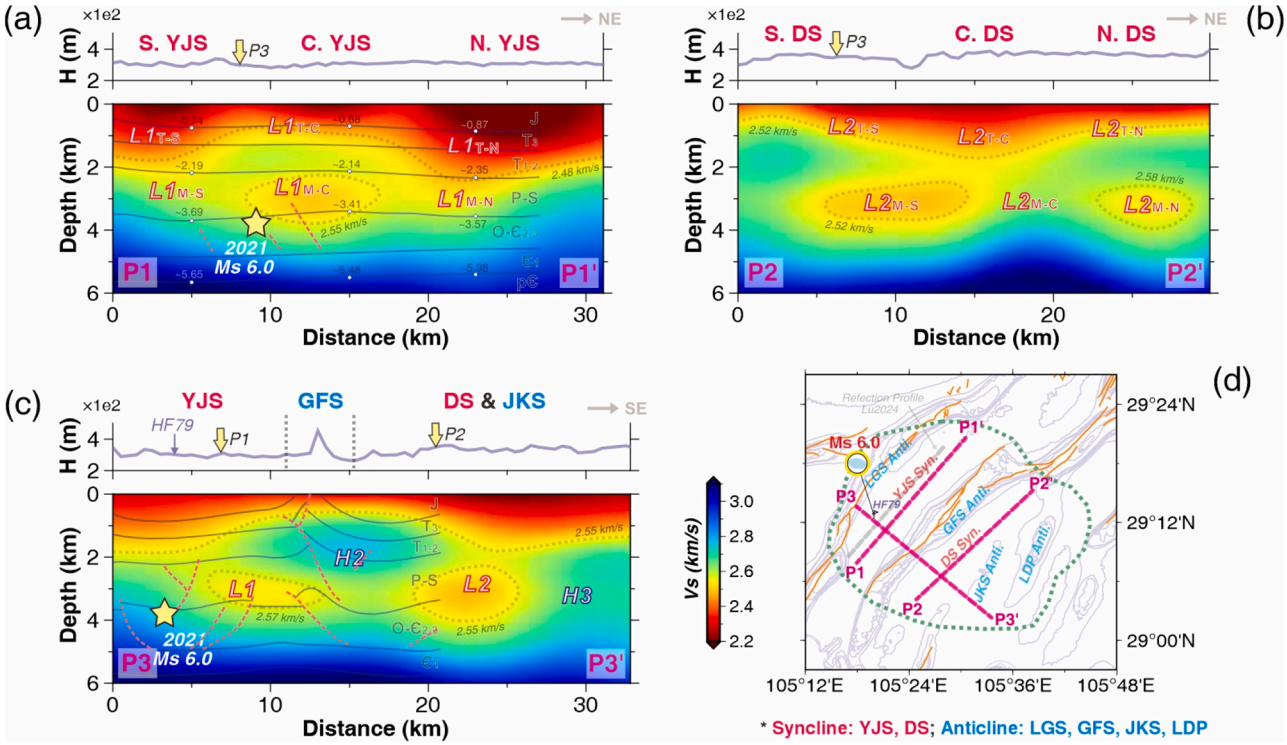

Fig. 4. Seismic tomographic images of sedimentary layers in Luxian County (vertical slices). Along-strike S-wave velocity variations are shown for the Yujiasi syncline **(a)** and the Desheng syncline **(b)**, with a NW–SE-trending profile crossing multiple anticlines and synclines presented in **(c)**. Topography along each profile is displayed above the corresponding subplot. The centroid of the 2021 Ms 6.0 Luxian earthquake is marked with a yellow star. Stratigraphic configurations (gray solid lines) and mapped faults (red dashed lines) in panels (a) and (c) are sourced from active-source seismic reflection surveys (Lu et al., 2024). Representative stratigraphic elevations for the northern, central, and southern Yujiasi syncline are labeled in panel (a). Seismic velocity contours are shown as gray dashed lines. The intra-Yujiasi seismic reflection profile, located ~4 km northwest of P1–P1', is indicated by the gray dashed line in panel (d) and its results are projected onto profile P1–P1'. Synclines and anticlines are indicated by pink and blue colors, respectively. **(d)** Map view showing the cross-section locations and major geological features. *pЄ*, Precambrian; $Є_1$, Lower Cambrian; $Є_{2-3}$, Upper–Middle Cambrian; *O*, Ordovician; *S*, Silurian; *P*, Permian; T_{1-2}, Lower–Middle Triassic; T_3, Upper Triassic; *J*, Jurassic.

amplitude of these anomalies also provide insights into the fine-scale internal structures of the synclines. At 1–2 km depth, corresponding to the Jurassic–Triassic terrestrial strata, the Yujiasi syncline exhibits strong low-velocity anomalies in its northern and southern segments (L1T-N and L1T-S) with magnitudes of up to ~10 %, whereas the central segment shows a weaker anomaly of only ~0–2 % (L1T-C). At 3–5 km depth, within the Permian–Cambrian marine strata, this pattern reverses: the central Yujiasi syncline hosts a stronger low-velocity anomaly (up to ~5 %; L1M-C), while the anomalies weaken toward the northern and southern segments (L1M-N and L1M-S). A comparable two-layer velocity structure also appears in the Desheng syncline (L2), characterized by strong low-velocity anomalies in the central part of the terrestrial strata (up to 4 %; L2T-C) and in the northern and southern portions of the marine strata (up to 8 %; L2M-N and L2M-S), with weaker anomalies elsewhere (L2T-N, L2T-S, L2M-C). Within the marine strata, the high-velocity Gufoshan anticline (H2) shows along-strike variations that positively correlate with surface topography. The strongest anomaly, reaching up to ~8 %, occurs in the northern segment, spatially coinciding with the widest exposed pre-Jurassic anticlinal core and the highest elevations. Because checkerboard tests show reduced resolution below 6 km (Fig. S12) and the available long-period (>6 s) data are insufficient to image the crystalline basement (Fig. S1d), our seismic interpretation is restricted to the sedimentary cover above this depth.

3.3. Source attributes of the local earthquakes

Of the thirteen moderate-magnitude earthquakes analyzed, eleven produced CMT solutions with satisfactory waveform fits (variance reduction: ~70–90 %; Table S1) and demonstrate robustness in the following tests. All solutions indicate reverse-faulting coseismic motion, and nine exhibit P-axis orientations of NWW–SEE (Figs. 2d and 5). These results are consistent with the NE–SW structural trend of the local tectonic framework and with most previously reported source parameters for earthquakes in the Yujiasi syncline (e.g., Lai et al., 2023; Mo et al., 2024). Two events (2022–08–19 07:07:36 and 2022–12–08 09:45:49) depart from this pattern, showing NE–SW-oriented P axes similar to that of the 2021 Ms 6.0 mainshock. Centroid depths for all events range from 1 to 6 km, placing them within the sedimentary cover.

To evaluate the robustness of the MT parameters, we performed four sets of tests. Test 1 applied an alternative band-pass filter (0.10–0.33 Hz) to assess the influence of frequency-dependent noise. Test 2 repeated the inversions using only deviatoric MTs, omitting the isotropic component. Test 3 adopts a pseudo-3D velocity model for calculating Green's functions, in which path-averaged velocity models specific to each source–station pair are used. Test 4 employed a bootstrap procedure: for each event, 100 inversions were run with 75 % of the available stations randomly selected, and the original station count was restored from these subsets. Figures S13 and 5 summarize the results, including Kagan angles and differences in the percentages of double-couple (DC), compensated linear vector dipole (CLVD), and isotropic (ISO) components between the test and final solutions. The consistently low Kagan angles (<10°) confirm the stability of the derived fault plane solutions, and the DC, CLVD, and ISO percentages remain stable across all tests for the eleven MT solutions. Further evaluation of the robustness of MT solutions to uncertainties in Earth structure would benefit from the incorporation of a fully 3D anisotropic Earth model.

Three events (highlighted in red in Fig. 5) exhibit significant non-DC

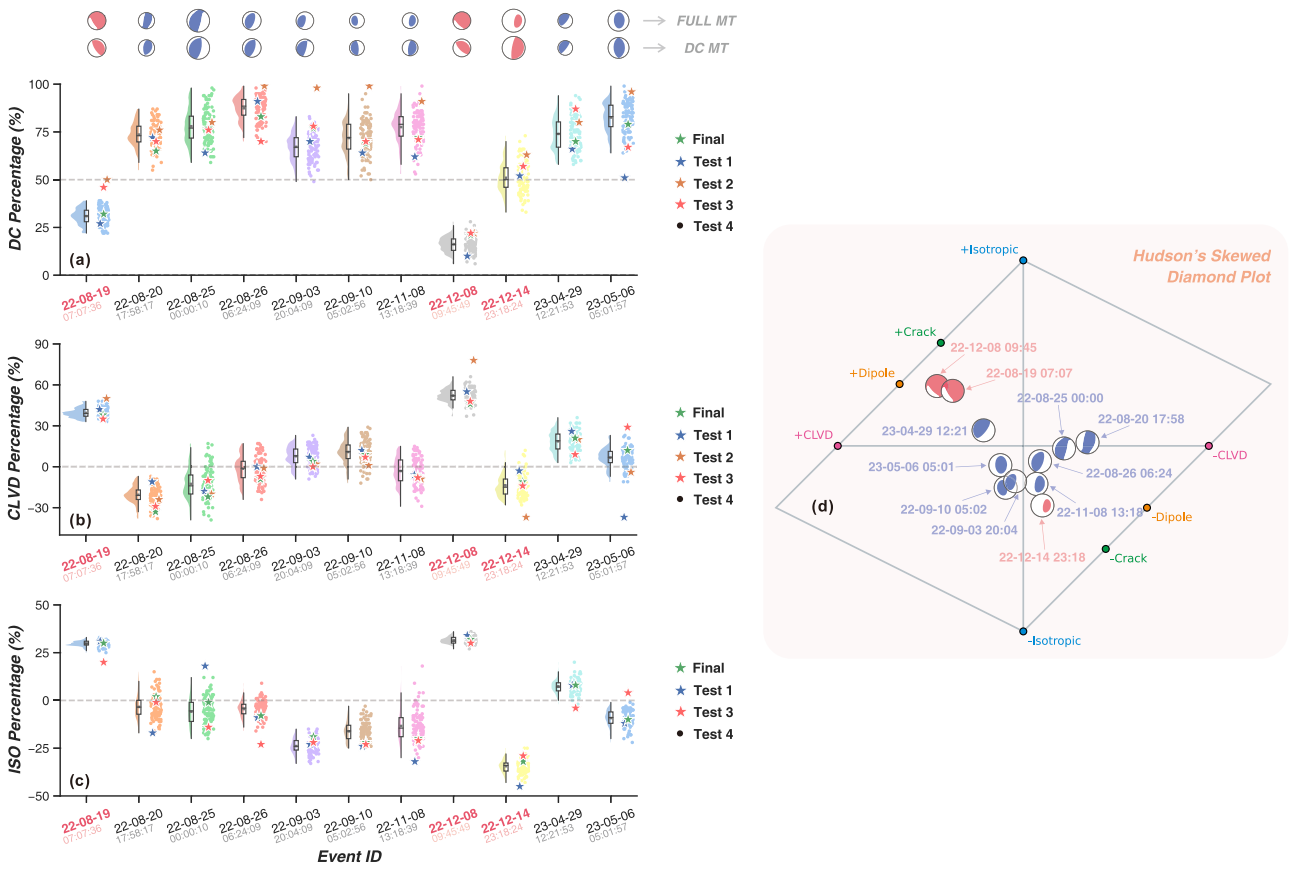

Fig. 5. Statistical summary of 11 new moment tensor solutions in Luxian County (MT decomposition). In panels **(a–c)**, Percentages of double-couple (DC), compensated linear vector dipole (CLVD), and isotropic (ISO) components are shown for the final inversion and four reliability tests. Final, Test 1, Test 2, Test 3 results are marked by green, blue, orange, and red stars, respectively. Test 4 results are displayed as raincloud plots showing the median (center line), mean (gray squares), interquartile range (boxes), and all individual measurements (colored dots). For Test 2, ISO percentages are omitted because the deviatoric MT inversion constrains the ISO component to zero. Three events exhibiting significant non-DC component are highlighted in red. Beachball diagrams for the full moment tensor and its DC component are shown at the top. A Hudson plot for MT decomposition is shown in panel (d).

components and are all located within seismicity cluster S1 of the Yujiasi syncline (Fig. 2b). Satellite imagery suggests that two wells near the hypocenters of these events were in the hydraulic fracturing operation cycle, although direct operational records are unavailable. Interestingly, two of these three events display positive CLVD and ISO values and are associated with the anomalous NE–SW P-axis orientations, whereas the remaining event shows negative CLVD and ISO values and an NWW–SEE P-axis orientation parallel to the regional stress field. Taken together, these observations hint at a possible relationship among the orientation of the seismogenic fault of moderate-to-large-magnitude earthquakes, the sign of the non-DC components, and hydraulic fracturing activity in the Luxian shale gas field. Tensile faulting that combines shear and tensile motions provides a physically plausible explanation for these observations, given the consistent signs of the CLVD and ISO components (Vavryčuk, 2011). In particular, elevated fluid overpressure, potentially related to fracking fluid injection, may have contributed to the two extensive tensile-faulting events occurring on NW–SE–trending faults. The limited number of events, however, precludes statistically robust conclusions. Future studies with a larger earthquake dataset are needed to further investigate the rupture complexity of induced seismicity. In the present analysis, we focus exclusively on the DC components of the MT solutions.

4. Discussion

4.1. Formation mechanisms of the synclinal low velocity anomalies

Beyond the first-order seismic velocity contrast between synclines and anticlines, our tomographic images reveal distinct two-layer velocity variations along the syncline axes (Figs. 3 and 4). At depths of 1–2 km, which correspond to the terrestrial sedimentary strata, the shape and amplitude of shallow intra-syncline low-velocity anomalies appear to reflect lateral differences in stratigraphic elevation. Within the Yujiasi syncline, for example, the velocity pattern indicates that the terrestrial strata occupy a relatively higher structural level in the central segment than in the northern and southern segments. This interpretation agrees with the ~100 ms advance in two-way traveltime of Triassic stratigraphic interfaces reported by seismic reflection surveys (Lu et al., 2024) (Fig. 4a). The stronger low-velocity anomalies in the northern and southern segments (L1T-N and L1T-S) therefore signify greater downward flexure of the strata, implying enhanced strain accommodation under the prevailing NWW-directed regional stress field compared with the central segment (Fig. 4a). This inference is further supported by along-strike variations in the width of the Yujiasi syncline with a wider thus relatively less deformed central segment (Fig. 1b). Collectively, these observations suggest that although the Luxian segment of the eastern Sichuan fold-and-thrust belt exhibits the overall character of a Jura-type ejective fold system with broad, gently folded synclines, significant spatial variations in strain intensity exist within individual synclines. From a seismological perspective, the lowest intra-syncline

strain appears to be concentrated in the central segment of the Yujiasi syncline and in the northern and southern segments of the Desheng syncline (Fig. 3c).

At depths of 3–6 km within the marine sedimentary strata, the along-strike stratigraphic configuration of the Yujiasi syncline gradually transitions into a southwestward-deepening geometry at its base due to the increasing thickness of Silurian–Cambrian strata in that direction (Lu et al., 2024) (Fig. 4a). The regional depocenter for these marine strata is located south of Luxian County (Yang et al., 2019). This, when combined with localized thickening near the décollement horizon (Tian et al., 2024a), likely explains the observed stratigraphic thickness variations. However, this stratigraphic trend does not match the seismic velocity pattern, indicating that factors beyond lithology significantly influence the synclinal velocity structure.

Interestingly, the lateral variations in intra-syncline low-velocity magnitudes at these depths display an inverse pattern relative to the overlying terrestrial strata. This relationship, seen in both the Yujiasi and Desheng synclines, also correlates closely with surface hypsometric integral variations (Zhou et al., 2022), implying a common tectonic mechanism acting throughout the sedimentary column, from the surface through the terrestrial to the marine strata. Physical experiments show that décollement depth exerts a first-order control on the structural style of Jura-type folds (Wu et al., 2019; Xie et al., 2013): shallow décollement layers favor ejective folds with low-strain synclines and narrow anticlines, whereas deeper layers promote trough-like folds with high-strain synclines and wide anticlines. In the Luxian region, major décollement layers, composed mainly of gypsum-salt, coal, mudstone, and shale, primarily occur at different stratigraphic levels within the marine strata: ~2 km in the Upper Permian–Lower Triassic, ~3 km in the Silurian, and ~5 km in the Middle–Lower Cambrian. Within the Yujiasi syncline, the former two sets of décollements preserve the pronounced variations in stratigraphic elevation observed in the overlying terrestrial strata, lying higher in the central segment and lower in the north and south (Fig. 4a). This contrast is especially marked near the 2021 Ms 6.0 mainshock rupture zone, where the Silurian décollements abruptly deepen south–southwestward. The resulting intra-syncline strain distribution, as predicted by physical modeling, aligns with geophysical and geological observations of terrestrial seismic velocity and synclinal width, underscoring the fundamental role of sedimentary décollements in controlling local deformation.

Because strain intensity is lower, large-scale penetrating faults are likely less developed in the central Yujiasi syncline and in the northern and southern segments of the Desheng syncline. This structural setting favors fluid and gas preservation, contributing to the observed strong low-velocity anomalies and the high productivity and enrichment of shale gas reservoirs in these areas. Supporting evidence of this scenario also comes from low-resistivity anomalies at 3–6 km depth in the central Yujiasi syncline, which are markedly stronger than those farther south (Liu et al., 2024a). Additionally, between the central and northern Yujiasi syncline, the contrast in stratigraphic elevation of the Cambrian décollement layers gradually diminishes and even slightly reverses with increasing depth (Fig. 4a). This pattern is also reflected in our 6 km depth tomographic slice (Fig. S14), where the velocity contrast between the two segments becomes indistinguishable. These observations suggest that décollement horizons exert their strongest control on the deformation style of the strata immediately above them, with diminishing influence at greater distances. In other words, the structural style of the terrestrial strata is governed primarily by the Permian–Triassic décollements, whereas the Cambrian décollements chiefly influence the deformation of the deeper marine strata.

4.2. Spatial relationship between seismic velocity and earthquake location

A compilation of local earthquake catalogs and focal mechanism solutions from this and previous studies is shown in Fig. 2. In the Yujiasi syncline, the abundance of seismicity data allows a detailed discussion of the local seismogenic environment when integrated with the newly derived seismic images. In contrast, seismicity in the Desheng syncline is relatively sparse due to catalog incompleteness and is discussed only in the context of potential seismic hazard.

Horizontally, post–shale gas exploitation seismicity in the Yujiasi syncline is concentrated in three distinct clusters. The northern cluster (S1) lies near the Gufoshan anticline and extends south-southwestward along a linear trend. The southern cluster (S2) spans the syncline width and extends north-northeastward, also forming a linear pattern. The southernmost cluster (S3) is located near the Luoguanshan anticline. Notably, clusters S1 and S2 are symmetrically distributed around a central seismic gap (G) in the heart of the syncline. Vertically, seismicity is mainly confined to marine sedimentary strata at depths of 3–7 km (Fig. 2c), consistent with observations from other shale gas fields in the southern Sichuan basin (Tan et al., 2020).

Focal mechanism solutions indicate that reverse faulting is the dominant rupture mode for moderate-to-large-magnitude earthquakes in Luxian County. Most P axes are oriented approximately NWW–SEE with near-horizontal plunges (~18°), aligning with the regional SHmax (Heidbach et al., 2018). However, anomalous P-axis orientations (N–S to NE–SW) are observed for eight events (highlighted in red; Fig. 2b), including four from the 2021 Ms 6.0 earthquake sequence in S2 and four additional events in S1 spanning a broader time range. Normal-faulting (n = 35; T axes oriented E–W to NE–SW) and strike-slip (n = 2) mechanisms appear exclusively among aftershocks of the 2021 Ms 6.0 event in S2 and S3, likely reflecting a temporary stress regime reversal due to the complete release of compressive stress during the mainshock (Wang et al., 2023).

Integrating seismic velocity and seismicity observations reveals a key feature: the occurrence of induced earthquakes, including microseismicity, moderate-magnitude events, and the 2021 Ms 6.0 mainshock is geographically biased in Luxian County, tending to cluster along the edges of low-velocity anomalies (See Fig. S15 for a quantitative demonstration). In the Yujiasi syncline for example, the central seismic gap (G) coincides with the core of a low-velocity anomaly within the marine sedimentary strata, the principal seismogenic layer.

While previous studies have also reported spatial alignment between seismicity and velocity anomalies, the specific observations and correlated features in this study differ. At 4–5 km depth, the 2021 Ms 6.0 mainshock and its aftershocks are bounded horizontally by a high-velocity zone to the west and a low-velocity zone to the east (Fig. 3c–d). This contrasts with earlier tomography results (e.g., Wu et al., 2024a; Xu et al., 2023), which identified the opposite velocity gradient and suggested preferential aftershock localization within the high-velocity zone. Notably, our velocity model aligns more closely with the continuation of anticline–syncline structures from the surface down to the Middle Cambrian Gaotai Formation (~5 km depth) shown by seismic reflection surveys (Lu et al., 2024; Tian et al., 2024a). The longer, 10-month recording duration of the ZJU–LX broadband seismometers, as compared to 1-month deployments of short-period large-N arrays, likely contributed to this improved correspondence.

4.3. Seismogenic environment of the Luxian shale gas field

The clustering of seismicity within marine strata can be attributed to elevated stratigraphic pressure, which promotes stress accumulation, and to the higher density of small-scale faults (Lu et al., 2024; Tian et al., 2024a). These pre-existing faults at depth are susceptible to reactivation under stress perturbations induced by industrial activities within the Wufeng–Longmaxi Formations, as well as by large earthquakes (Zhu et al., 2025). Various triggering mechanisms may contribute to the reactivation, including pore pressure diffusion, poroelastic stress transfer, and loading induced by aseismic slip (Atkinson et al., 2020; Bao and Eaton, 2016; Cheng et al., 2016; Eyre et al., 2019; Moein et al., 2023; Schultz et al., 2020; Yu et al., 2021).

Horizontally, many earthquakes appear to occur on fold-

accommodation faults that accommodate the ongoing NWW–SEE-directed compressive forces in the eastern Sichuan fold-and-thrust belt. Supporting evidence includes (1) NNE–SSW-trending seismicity lineaments in clusters S1 and S2 that align with anticline–syncline transitions (Fig. 2a), (2) predominantly reverse-faulting mechanisms with fold-normal P axes (Fig. 2d), and (3) northwestward-dipping geometry of seismicity in cluster S1 (Guo et al., 2025).

Significant reverse-faulting earthquakes, including the 2021 Ms 6.0 sequence, also occur on intra-syncline faults with fold-normal planes. These faults preferentially develop under a localized NEE-directed compressive stress regime caused by heterogeneous deformation between syncline segments (Fig. 6). High-strain segments undergo stronger deformation, leading to along-strike material extrusion and compression toward adjacent low-strain segments (Wang et al., 2023). This differential deformation reorients the local SHmax in the contact zone into a fold-parallel direction, promoting stress accumulation and the development of fold-normal faults.

The main bodies of seismicity clusters S1 and S2 are located at intersections between anticline–syncline structural transitions and high- to low-strain transitions within synclines. These locations represent transitional stress regimes and are characterized by increased strata geometric complexity. In such settings, the two principal stresses are of comparable magnitudes, facilitating easier seismicity triggering of the abundant pre-existing faults across a broad range of fault plane orientations (Han and van der Baan, 2025; Lai et al., 2023).

Approximately 70 % of the newly reported moderate-magnitude earthquakes, as well as the 2021 Ms 6.0 event (Lai et al., 2023), have focal depths greater than their centroid depths (Table S1), possibly related to continuous loading of pore fluid pressure near the deeper ends of faults by industrial operations (Tian et al., 2024b). For example, the 2021 Ms 6.0 earthquake in cluster S2 nucleated near the deeper terminus of the seismogenic fault close to the basement décollement (~6 km), and was probably triggered by fluid diffusion from hydraulic fracturing at well pad H79 (Zhao et al., 2023b). In comparison, two newly reported moderate-magnitude events with fold-normal fault planes in cluster S1 (2022–08–19 07:07:36 and 2022–12–08 09:45:49) initiated within the gas-rich Silurian layers and only ruptured faults extending upward into terrestrial strata, with limited downward propagation through the marine strata. A possible explanation for this difference is that the reduced curvature of the deep-marine décollement layers at the cluster S1 location limits the development of deep-seated fold-normal faults. Nevertheless, the occurrence of a Mw 3.0 event (2021–08–15; labeled '1′ in Figs. 2b and S14b) at ~6 km depth indicates that the seismogenic potential of the deep-marine strata beneath cluster S1 still warrants careful assessment for future damaging earthquakes.

Hydraulic fracturing operations are ongoing not only in the Yujiasi syncline but also in the Desheng syncline, where passive seismic constraints remain limited. In this study, in addition to low-velocity anomaly L1 in Yujiasi, we identify a comparable low-velocity anomaly L2 in Desheng. The Sanxikou reservoir, a medium-sized facility with ~40 million m^3 storage, lies above the southeastern edge of L2M-N, marking a high-risk location. The spatial control of heterogeneous folding on induced seismicity revealed in this study can inform hydraulic fracturing planning in the southern Sichuan basin, particularly within the eastern Sichuan fold-and-thrust belt. To mitigate the risk of induced earthquakes, continuous monitoring of local seismicity and detailed mapping of deep active faults are essential. Special attention should be given to edge zones of low seismic velocity within marine sedimentary strata to optimize traffic light protocols and enhance risk management.

A broader implication of the spatially biased distribution of induced seismicity documented in this study is that tectonic factors serve as critical controls on the susceptibility to anthropogenically induced earthquakes, although the governing mechanisms may vary by region; for example, in central Alberta, higher earthquake hazard susceptibility has been associated with reef margin settings and formation overpressure (Eaton and Schultz, 2018; Schultz et al., 2016). Integrating multiple geophysical (e.g., Vs) and geological (e.g., lithium concentration) proxies that reflect conditions favorable for induced seismicity (e.g., abundant preexisting faults, near-critical stress states, and hydraulic connectivity) within a machine learning framework (Pawley et al., 2018) could further enhance the assessment of seismogenic potential in industrial production fields in the southern Sichuan Basin.

5. Conclusions

Using the newly deployed ZJU–LX seismic array, we constructed a new S-wave velocity model (0–6 km depth) for the Luxian shale gas field, a strategically important shale gas production area in the southern Sichuan basin known by abundant reserves and favorable reservoir properties. The model reveals a two-layer sedimentary structure within regional synclines characterized by low-velocity anomalies. Lateral variations in anomaly amplitudes show opposite patterns between the upper terrestrial strata and the underlying marine strata, reflecting differences in stratigraphic elevation and fluid content. These features are likely controlled by heterogeneous strain intensity linked to variations in the depth of décollement layers.

We also identify moderate-magnitude earthquakes with anomalous

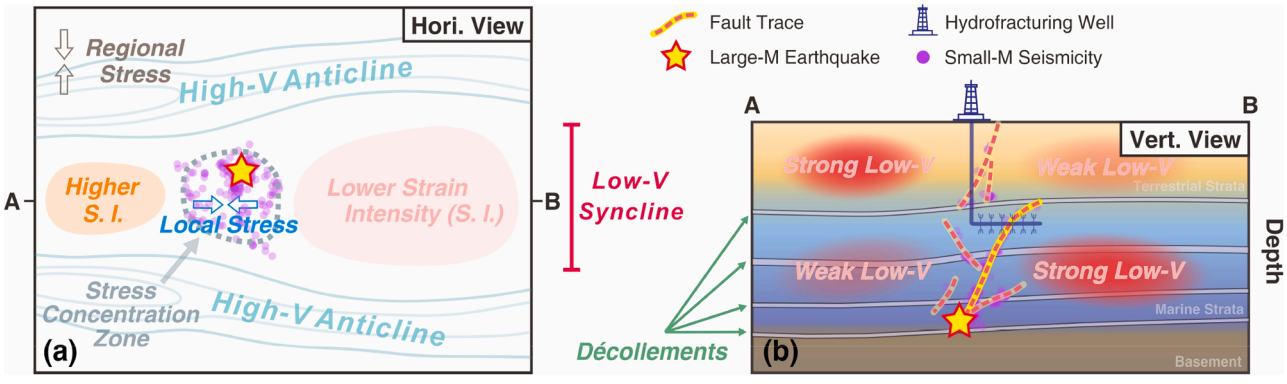

Fig. 6. Conceptual cartoons illustrating the seismogenic environment for moderate-to-large-magnitude earthquakes with fold-parallel P axes in the Luxian shale gas field. Regional compression fosters the development of alternating anticlines and synclines, expressed as first-order seismic-velocity perturbations within the sedimentary strata. Within synclines, depth variations of the décollement layers drive heterogeneous folding and shortening, producing along-strike differences in stratigraphic elevation and fluid content in the terrestrial and marine strata, respectively. These contrasts appear as along-strike changes in the amplitude of synclinal low-velocity anomalies. Heterogeneous folding also localizes stress and promotes the formation of fold-normal fault planes in intra-syncline strain transition zones, which are susceptible to triggering by hydraulic fracturing activities. The likelihood of moderate-to-large-magnitude induced earthquakes is high in the deep-marine strata there due to elevated stratigraphic pressure. Figures are schematic and not to scale.

NNE–SSW-oriented P axes, similar to the 2021 Ms 6.0 event, approximately 16 km to the northeast. Integrating seismic velocity with earthquake locations and source parameters demonstrates that earthquakes preferentially cluster along the edges of low-velocity anomalies within the marine strata, corresponding to synclinal transition zones of heterogeneous folding and shortening. Collectively, these findings provide new insights into the seismogenic environment and potential seismic hazards of the Luxian shale gas field and highlight the need for continued monitoring of seismic activity along the low-velocity margins of shale gas production areas in the southern Sichuan basin.

Data resources

The sedimentary shear-wave velocity model and moment tensor solutions for Luxian shale gas field are provided in the Supplementary Materials. The ZJU–LX seismic array data are available from the corresponding author upon reasonable request.

CRediT authorship contribution statement

Bingfeng Zhang: Writing – review & editing, Writing – original draft, Visualization, Methodology, Investigation, Formal analysis, Data curation. **Xuewei Bao:** Writing – review & editing, Supervision, Project administration, Funding acquisition, Data curation, Conceptualization. **Mengfan Jiang:** Data curation. **Kecheng Zhou:** Data curation.

Declaration of competing interest

The authors declare that they have no known competing financial interests or personal relationships that could have appeared to influence the work reported in this paper.

Acknowledgements

We are grateful to Huili Guo, Yuejun Lü and Xinwei Li for providing the seismicity data. The DSurfTomo and BayesISOLA packages are freely accessible at https://github.com/HongjianFang/DSurfTomo and https://github.com/vackar/BayesISOLA, respectively. This work is funded by the National Natural Science Foundation of China under grant nos. U22B6002 and 42374055, 41774045. The authors thank Editor Hans Thybo, Ryan Schultz, and an anonymous reviewer for their constructive comments, which substantially improved the manuscript.

Supplementary materials

Supplementary material associated with this article can be found, in the online version, at doi:10.1016/j.epsl.2026.119860.

Data availability

Data will be made available on request.

References

Atkinson, G.M., Eaton, D.W., Igonin, N., 2020. Developments in understanding seismicity triggered by hydraulic fracturing. Nat. Rev. Earth Environ. 1, 264–277.
Bao, X., Eaton, D.W., 2016. Fault activation by hydraulic fracturing in western Canada. Science 354, 1406–1409.
Bao, X., Song, X., Li, J., 2015. High-resolution lithospheric structure beneath Mainland China from ambient noise and earthquake surface-wave tomography. Earth Planet. Sci. Lett. 417, 132–141.
Bensen, G.D., Ritzwoller, M.H., Barmin, M.P., Levshin, A.L., Lin, F., Moschetti, M.P., Shapiro, N.M., Yang, Y., 2007. Processing seismic ambient noise data to obtain reliable broad-band surface wave dispersion measurements. Geophys. J. Int. 169, 1239–1260.
Bouchon, M., 1981. A simple method to calculate Green's functions for elastic layered media. Bull. Seismol. Soc. Am. 71, 959–971.
Cai, G., Wang, W., Wu, J., Lai, G., Zhang, L., Bao, J., Liu, H., 2024. Three-dimensional velocity structure of the Ms 6.0 Luxian earthquake source region and adjacent areas based on a dense seismic array. Phys. Earth Planet. Inter. 357, 107281.
Chen, C., Zhang, R., Qiang, Z., LI, D., Xu, Z., 2022. Seismicity and three-dimensional crustal structure of the Luzhou region in the southern Sichuan Basin. China. Chin. J. Geophys. 65, 4672–4684.
Cheng, H., Zhang, H., Shi, Y., 2016. High-Resolution Numerical Analysis of the Triggering Mechanism of M L5.7 Aswan Reservoir Earthquake Through Fully Coupled Poroelastic Finite Element Modeling. Pure Appl. Geophys. 173, 1593–1605.
Eaton, D.W., Schultz, R., 2018. Increased likelihood of induced seismicity in highly overpressured shale formations. Geophys. J. Int. 214, 751–757.
Eyre, T.S., Eaton, D.W., Garagash, D.I., Zecevic, M., Venieri, M., Weir, R., Lawton, D.C., 2019. The role of aseismic slip in hydraulic fracturing–induced seismicity. Sci. Adv. 5, eaav7172.
Fang, H., Yao, H., Zhang, H., Huang, Y.-C., van der Hilst, R.D., 2015. Direct inversion of surface wave dispersion for three-dimensional shallow crustal structure based on ray tracing: methodology and application. Geophys. J. Int. 201, 1251–1263.
Grandin, R., Vallée, M., Lacassin, R., 2017. Rupture process of the Mw 5.8 Pawnee, Oklahoma, earthquake from Sentinel-1 InSAR and seismological data. Seismol. Res. Lett. 88, 994–1004.
Guo, H., Li, D., Wu, P., Yang, Q., Jiang, N., Gao, M., Ding, Z., 2025. High resolution catalog of the Luxian (Sichuan, China) Ms6.0 earthquake sequence and analysis of the seismogenic structures. Earthq. Sci. 38, 33–46.
Han, H., van der Baan, M., 2025. State of in situ stress and implications for fault slip potential in the Montney Play, Western Canada. J. Geophys. Res.: Solid Earth 130, e2024JB030976.
Hao, S., Chen, J., Xu, M., Tong, P., 2024. Topography-incorporated adjoint-state surface wave traveltime tomography: method and a case study in Hawaii. J. Geophys. Res.: Solid Earth 129, e2023JB027454.
Hasterok, D., Halpin, J.A., Collins, A.S., Hand, M., Kreemer, C., Gard, M.G., Glorie, S., 2022. New maps of global geological provinces and tectonic plates. Earth-Sci. Rev. 231, 104069.
Heidbach, O., Rajabi, M., Cui, X., Fuchs, K., Müller, B., Reinecker, J., Reiter, K., Tingay, M., Wenzel, F., Xie, F., Ziegler, M.O., Zoback, M.-L., Zoback, M., 2018. The World Stress Map database release 2016: crustal stress pattern across scales. Tectonophysics 744, 484–498.
Herrmann, R.B., 2013. Computer Programs in Seismology: an evolving tool for instruction and research. Seismol. Res. Lett. 84, 1081–1088.
Keranen, K.M., Weingarten, M., 2018. Induced seismicity. Annu Rev. Earth. Planet. Sci. 46, 149–174.
Lai, G., Jiang, C., Wang, W., Lei, X., Zhang, L., Cai, G., Gong, H., Guo, X., Chen, M., 2023. Spatial–temporal distribution and focal mechanisms for the shallow earthquakes in the Rongchang-Luxian region in southern Sichuan Basin, China. Seismol. Res. Lett. 94, 1860–1876.
Lei, X., Su, J., Wang, Z., 2020. Growing seismicity in the Sichuan Basin and its association with industrial activities. Sci. China Earth Sci. 63, 1633–1660.
Lei, X., Yu, G., Ma, S., Wen, X., Wang, Q., 2008. Earthquakes induced by water injection at 3 km depth within the Rongchang gas field, Chongqing, China. J. Geophys. Res. 113, B10310.
Li, C., He, D., Sun, Y., He, J., Jiang, Z., 2015. Structural characteristic and origin of intracontinental fold belt in the eastern Sichuan basin, South China Block. J. Asian Earth Sci. 111, 206–221.
Li, J., Xu, J., Zhang, H., Yang, W., Tan, Y., Zhang, F., Meng, L., Zang, Y., Miao, S., Guo, C., Li, Z., Lu, R., Sun, J., 2023. High seismic velocity structures control moderate to strong induced earthquake behaviors by shale gas development. Commun. Earth Environ. 4, 188.
Li, X., Zhang, G., Xie, Z., Li, S., Lü, Y., 2022. Seismogenic mechanism of the 2021 M6.0 luxian earthquake and seismicity spatio-temporal characteristics around the source region. Chin. J. Geophys. 65, 4284–4298.
Liu, G., Lu, R., He, D., Tao, W., Su, P., Zhang, W., Zhang, J., Xu, F., Sun, X., Wang, W., 2023. Detailed imaging of a seismogenic fault that potentially induced the two 2019 Weiyuan moderate earthquakes in the Sichuan basin, China. Seismol. Res. Lett. 94, 1379–1391.
Liu, X., Zhan, Y., Zhao, L., Sun, X., Lou, X., 2024a. Using resistivity structure to study the seismogenic mechanism of the 2021 Luxian Ms6.0 earthquakes. Remote Sens. (Basel) 16, 4116.
Liu, Z., Chen, Z., Li, Y., Zhao, Z., Hong, S., Hu, L., Ma, L., Lu, C., Zhao, Y., He, H., Su, S., Zhao, Y., Shao, W., Cao, Z., Wang, H., 2024b. Shale gas leakage and fault activation: insight from the 2021 Luxian MS 6.0 earthquake, China. Tectonophysics 891, 230530.
Lu, R., He, D., Liu, J.-Z., Tao, W., Huang, H., Xu, F., Liu, G., 2021. Seismogenic faults of the Changning earthquake sequence constrained by high-resolution seismic profiles in the southwestern Sichuan basin, China. Seismol. Res. Lett. 92, 3757–3766.
Lu, R., Jiang, C., He, D., Wang, W., Guo, Z., Zhang, W., Tao, W., Yang, X., Lai, G., Zhan, Y., Liu, G., Xu, F., Sun, X., 2024. Seismogenic fault of the 2021 Ms 6.0 Luxian induced earthquake in the Sichuan Basin, China constrained by high-resolution seismic reflection and dense seismic array. J. Struct. Geol. 179, 105050.
Luu, K., 2023. Evodcinv: inversion of dispersion curves using evolutionary algorithms.
Mo, L., Chu, R., Gu, W., Sheng, M., Ma, H., Li, X., 2024. Research on the source parameters of the 2021 Luxian Ms6.0 earthquake. Chin. J. Geophys. 67, 1487–1500.
Moein, M.J.A., Langenbruch, C., Schultz, R., Grigoli, F., Ellsworth, W.L., Wang, R., Rinaldi, A.P., Shapiro, S., 2023. The physical mechanisms of induced earthquakes. Nat. Rev. Earth Environ. 4, 847–863.
Nie, H., Dang, W., Zhang, K., Su, H., Ding, J., Li, D., Liu, X., Li, P., Li, P., Yang, S., Zhao, J., Liu, M., Chen, Q., Sun, C., Wang, P., Liu, Z., 2024. Two decades of shale gas research & development in China: review and prospects. Nat. Gas Ind. 44, 20–52.

Paige, C.C., Saunders, M.A., 1982. LSQR: an algorithm for sparse linear equations and sparse least squares. ACM Trans. Math. Softw. 8, 43–71.
Pavlis, G.L., Vernon, F.L., 2010. Array processing of teleseismic body waves with the USArray. Comput. Geosci. 36, 910–920.
Pawley, S., Schultz, R., Playter, T., Corlett, H., Shipman, T., Lyster, S., Hauck, T., 2018. The geological susceptibility of induced earthquakes in the Duvernay play. Geophys. Res. Lett. 45, 1786–1793.
Rawlinson, N., Sambridge, M., 2004. Wave front evolution in strongly heterogeneous layered media using the fast marching method. Geophys. J. Int. 156, 631–647.
Schultz, R., Corlett, H., Haug, K., Kocon, K., MacCormack, K., Stern, V., Shipman, T., 2016. Linking fossil reefs with earthquakes: geologic insight to where induced seismicity occurs in Alberta. Geophys. Res. Lett. 43, 2534–2542.
Schultz, R., Skoumal, R.J., Brudzinski, M.R., Eaton, D., Baptie, B., Ellsworth, W., 2020. Hydraulic fracturing-induced seismicity. Rev. Geophys. 58, e2019RG000695.
Sheng, M., Chu, R., Peng, Z., Wei, Z., Zeng, X., Wang, Q., Wang, Y., 2022. Earthquakes triggered by fluid diffusion and boosted by fault reactivation in Weiyuan, China due to hydraulic fracturing. J. Geophys. Res.: Solid Earth 127, e2021JB022963.
Sokos, E.N., Zahradnik, J., 2008. ISOLA a Fortran code and a Matlab GUI to perform multiple-point source inversion of seismic data. Comput. Geosci. 34, 967–977.
Song, J., Zhu, W., Zi, J., Yang, H., Chu, R., 2025. An enhanced focal mechanism catalog of induced earthquakes in Weiyuan, Sichuan, from dense array data and a multitask deep learning model. Seism. Rec. 5, 175–184.
Tan, Y., Hu, J., Zhang, H., Chen, Y., Qian, J., Wang, Q., Zha, H., Tang, P., Nie, Z., 2020. Hydraulic fracturing induced seismicity in the southern Sichuan Basin due to fluid diffusion inferred from seismic and injection data analysis. Geophys. Res. Lett. 47, e2019GL084885.
Tian, F., Liang, H., Zang, D., Liu, H., Wu, F., He, D., Liu, P., Liu, Z., Zhang, W., Si, Y., Chen, H., 2024a. Structural characteristics of strike-slip faults in the Luzhou-Yunjin area, southern Sichuan Basin. Chin. J. Geol. 59, 804–818.
Tian, W., Wu, Q., Dai, K., Guo, R., Yao, Z., Qiang, Z., Deng, F., 2024b. Seismological evidence for the existence of long-distance hydrological channel and its implication for fluid overpressure in southern Sichuan, China. Geophys. Res. Lett. 51, e2023GL107167.
Vackář, J., Burjánek, J., Gallovič, F., Zahradník, J., Clinton, J., 2017. Bayesian ISOLA: new tool for automated centroid moment tensor inversion. Geophys. J. Int. 210, 693–705.
Vavryčuk, V., 2011. Tensile earthquakes: theory, modeling, and inversion. J. Geophys. Res. 116, B12320.
Wang, C., Liang, C., Liao, J., Yao, Z., Xu, R., Yang, Y., 2023. Temporary stress regime reversal immediately after the complete release of the localized compressive stress by the 2021 Luxian Ms 6.0 earthquake, Sichuan Basin. Earth Planet. Sci. Lett. 618, 118282.
Wang, M., Shen, Z.K., 2020. Present-day crustal deformation of continental China derived from GPS and its tectonic implications. J. Geophys. Res.: Solid Earth 125, e2019JB018774.
Wang, M., Yang, H., Fang, L., Han, L., Jia, D., Jiang, D., Yan, B., 2020. Shallow faults reactivated by hydraulic fracturing: the 2019 Weiyuan earthquake sequences in Sichuan, China. Seismol. Res. Lett. 91, 3171–3181.
Wu, H., Qiu, N., Chang, J., Zhang, J., Wang, Y., 2019. Physical simulation on development of multilayer detachment fold belt in eastern Sichuan. Earth Sci. 44, 784–797.
Wu, J., Tan, J., Xu, J., Li, L., Beroza, G.C., Mumford, K.G., Van De Ven, C., Chen, B., Elsworth, D., 2025. Challenges to sustainable large-scale shale gas development in China. Proc. Natl. Acad. Sci. U.S.A 122, e2415192122.
Wu, P., Guo, H., Xu, W., Qin, T., Li, D., Lu, L., Ding, Z., 2024a. High-resolution velocity and seismic anisotropy structures of the 2021 Ms 6.0 Luxian earthquake zone in Sichuan Basin. Seismol. Res. Lett. 96, 78–96.
Wu, P., Li, D., Zhan, Y., Guo, H., Liu, X., Xu, W., Yang, Q., Lu, L., Ding, Z., 2023. Three-dimensional fine S-wave velocity structure around the source area of the Sichuan Luxian Ms6.0 earthquake on September 16, 2021. Chin. J. Geophys. 66, 2386–2403.
Wu, X., Xu, X., Yu, G., Ren, J., Yang, X., Chen, G., Xu, C., Du, K., Huang, X., Yang, H., Li, K., Hao, H., 2024b. The China Active Faults Database (CAFD) and its web system. Earth Syst. Sci. Data 16, 3391–3417.
Xie, G., Jia, D., Zhang, Q., Wu, X., Shen, L., Lü, Y., Zou, X., 2013. Physical modeling of the Jura-type folds in Eastern Sichuan. Acta Geol. Sin. 87, 773–788.
Xu, W., Wu, P., Li, D., Guo, H., Yang, Q., Lu, L., Ding, Z., 2023. Joint inversion of Rayleigh group and phase velocities for S-wave velocity structure of the 2021 Ms6.0 Luxian earthquake source area, China. Earthq. Sci. 36, 356–375.
Yang, H., Zhao, S., Liu, Y., Wu, W., Xia, Z., Wu, T., Luo, C., Fan, T., Yu, L., 2019. Main controlling factors of enrichment and high-yield of deep shale gas in the Luzhou Block, southern Sichuan Basin. Nat. Gas Ind. 39, 55–63.
Yi, G., Zhao, M., Long, F., Liang, M., Wang, M., Zhou, R., Wang, S., 2021. Characteristics of the seismic sequence and seismogenic environment of the Ms6.0 Sichuan Luxian earthquake on September 16, 2021. Chin. J. Geophys. 64, 4449–4461.
Yin, G., Zhang, H., Guo, Z., He, L., Chu, R., Guo, Y., Tang, M., Zhang, Y., Shi, Y., 2025. Long-term effects on earthquakes induced by poroelastic effect and fluid diffusion during shale gas production in Rongchang, China. Tectonophysics 916, 230927.
Yu, H., Harrington, R.M., Kao, H., Liu, Y., Wang, B., 2021. Fluid-injection-induced earthquakes characterized by hybrid-frequency waveforms manifest the transition from aseismic to seismic slip. Nat. Commun. 12, 6862.
Zhao, B., 2024. A relocated earthquake catalog in Sichuan region (2010–2023) based on a three-dimensional velocity model.
Zhao, J., Jiao, L., Lei, Y., Tu, J., 2023a. Unmanned aerial vehicle aeromagnetic analyses reveal the causative faults and seismogenic mechanism of the 2021 Ms 6.0 Luxian, China, earthquake. Seismol. Res. Lett. 94, 2627–2641.
Zhao, Y., Jiang, G., Lei, X., Xu, C., Zhao, B., Qiao, X., 2023b. The 2021 Ms 6.0 Luxian (China) earthquake: blind reverse-fault rupture in deep sedimentary formations likely induced by pressure perturbation from hydraulic fracturing. Geophys. Res. Lett. 50, e2023GL103209.
Zhou, W., Lanza, F., Grigoratos, I., Schultz, R., Cousse, J., Trutnevyte, E., Muntendam-Bos, A., Wiemer, S., 2024. Managing induced seismicity risks from enhanced geothermal systems: a good practice guideline. Rev. Geophys. 62, e2024RG000849.
Zhou, W., Liang, M., Zuo, H., Liao, C., Wu, W., Wang, M., Gong, Y., Wei, Y., 2022. Response of the topography of Laixihe drainage to the structural deformation induced by Ms6.0 Luxian earthquake and its indication. Acta Seismol. Sin. 44, 250–259.
Zhu, A., Li, Y., Chen, Q., Li, J., Li, X., 2025. Coseismic stress and fluid-driven aftershocks sequence of the 2021 Ms 6.0 earthquake in Luxian, Sichuan, China. Earth Planet. Sci. Lett 668, 119571.
Zi, J., Yang, Y., Yang, H., Su, J., 2025. The 11-month precursory fault activation of the 2019 ML 5.6 earthquake in the Weiyuan shale gas field, China. Commun. Earth Environ. 6, 175.
Zuo, K., Zhao, C., 2023. Seismicity and seismogenic mechanism of the Ms 6.0 Luxian earthquake on September 16, 2021. Earthq. Res. Adv. 3, 100253.